UC Berkeley
UC Berkeley Previously Published Works

Title

Combinatorial alloying improves bismuth vanadate photoanodes via reduced monoclinic distortion

Permalink

Journal

ISSN

Authors

Newhouse, PF
Guevarra, D
Umehara, M
et al.

Publication Date

2018

DOI

Peer reviewed

PAPER

Check for updates

Combinatorial alloying improves bismuth vanadate photoanodes *via* reduced monoclinic distortion†

P. F. Newhouse,[a] D. Guevarra,[a] M. Umehara, [ID] [ab] S. E. Reyes-Lillo, [ID] [cde]
L. Zhou, [ID] [a] D. A. Boyd,[a] S. K. Suram,[a] J. K. Cooper, [ID] [cf] J. A. Haber,[a]
J. B. Neaton*[cegh] and J. M. Gregoire [ID] *[a]

Improving the efficiency of solar-powered oxygen evolution is both critical for development of solar fuels technologies and challenging due to the broad set of properties required of a solar fuels photo-anode. Bismuth vanadate, in particular the monoclinic clinobisvanite phase, has received substantial attention and has exhibited the highest radiative efficiency among metal oxides with a band gap in the visible range. Efforts to further improve its photoelectrochemical performance have included alloying one or more metals onto the Bi and/or V sites, with progress on this frontier stymied by the difficulty in computational modelling of substitutional alloys and the high dimensionality of co-alloying composition spaces. Since substitutional alloying concurrently changes multiple materials properties, understanding the underlying cause for performance improvements is also challenging, motivating our application of combinatorial materials science techniques to map photoelectrochemical performance of 948 unique bismuth vanadate alloy compositions comprising 0 to 8% alloys of P, Ca, Mo, Eu, Gd, and W along with a variety of compositions from each pairwise combination of these elements. Upon identification of substantial improvements in the (Mo,Gd) co-alloying space, structural mapping was performed to reveal a remarkable correlation between performance enhancement and a lowered monoclinic distortion. First-principles density functional theory calculations indicate that the improvements are due to a lowered hole effective mass and hole polaron formation energy, and collectively, our results identify the monoclinic distortion as a critical parameter in the optimization and understanding of bismuth vanadate-based photoanodes.

Broader context

Energy technologies are largely enabled by high performance functional materials, whose optimization requires tuning of a variety of underlying fundamental properties through strategies such as doping or alloying with additional elements. Alloying with multiple elements offers particular promise for simultaneously optimizing multiple properties, and while this materials development strategy can be applied broadly across energy technologies, its use is hampered by the vast materials search space and high expense of computational exploration. We present methodologies for parallel synthesis of 15 co-alloying composition spaces based on a target host compound, in this case the solar fuels photoanode $BiVO_4$. Integration of combinatorial experiments and first principles calculations yields not only the discovery of new optimal solar fuels photoanodes but also identification of the improvement mechanisms. The results demonstrate that, contrary to popular belief, a lowered monoclinic distortion is beneficial for carrier transport in bismuth vanadate, which is realized by combining a conductivity enhancing element such as Mo and a structural tuning element such as Gd. The alloy discovery and optimization methods offer a platform for accelerated development and understanding of complex energy materials.

[a] Joint Center for Artificial Photosynthesis, California Institute of Technology, Pasadena, CA 91125, USA. E-mail: gregoire@caltech.edu

[b] Future Mobility Research Department, Toyota Research Institute of North America, Ann Arbor, MI 48105, USA

[c] Joint Center for Artificial Photosynthesis, Lawrence Berkeley National Laboratory, Berkeley, CA 94720, USA

[d] Departamento de Ciencias Físicas, Universidad Andres Bello, Santiago 837-0136, Chile

[e] Department of Physics, University of California, Berkeley, California 94720, USA

[f] Chemical Sciences Division, Lawrence Berkeley National Laboratory, Berkeley, CA 94720, USA. E-mail: jbneaton@lbl.gov

[g] Molecular Foundry, Lawrence Berkeley National Laboratory, Berkeley, CA 94720, USA

[h] Kavli Energy NanoSciences Institute, Berkeley, CA 94720, USA

† Electronic supplementary information (ESI) available: Optical characterization, alternate visual representation of optical-structural-photoelectrochemical data, detailed computational results. See DOI: 10.1039/c8ee00179k

Introduction

The production of fuels *via* photoelectrochemistry (PEC) has been recognized as a promising method for capturing and storing intermittent solar energy, in particular as renewable transportation fuels.[1] Regardless of the fuel to be generated, the oxygen evolution reaction at the photoanode is critical; hence development of stable, efficient, n-type semiconductors composed of earth abundant elements and producible by scalable, cost-effective methods has received increasing research attention.[2–4] Bismuth vanadate, $BiVO_4$, in particular has become the oxide semiconductor serving as the platform to develop and demonstrate a toolkit of techniques for improving and understanding the fundamental properties and photoelectrochemical performance of novel oxide-based semiconductors, despite its non-optimal bandgap.[2,5] As recently reviewed, the methods of improving the properties include heterojunction formation, alloying or doping, hydrogen or nitrogen annealing, nanostructuring to enhance charge collection, microstructuring for photon management, and surface coating to passivate surface defects and enhance catalysis.[3,4,6–9]

The highest performing $BiVO_4$-based photoanodes reported to date have all incorporated several of these strategies in order to produce photocurrent densities in the range of approximately 2–6.7 mA cm^{-2} under AM 1.5 illumination, approaching the theoretical limit of 7.5 mA cm^{-2} for a semiconductor with 2.4 eV band gap.[2,3] Although to produce record, or near-record, performance it is necessary to simultaneously utilize multiple performance-enhancing methods, this approach inhibits an effort to understand the underlying principles governing the performance improvement from a particular modification. Indeed, application of multiple performance enhancing techniques while varying one parameter (*e.g.* alloying composition), can mask underlying performance trends if a non-varying technique (*e.g.* catalyst surface coating) is incompatible with the given alloy compositions. Therefore, in this study we focus on understanding the improvements in PEC performance produced by alloying multiple elements, both individually and in combination, with optimization of photoactivity compromising an important but secondary consideration. We begin by systematically synthesizing and evaluating a library of 948 $BiVO_4$ alloys containing various amounts of P, Ca, Mo, Eu, Gd, and W, as well as their pairwise combinations, and additionally perform high throughput optical and structural characterization to map their relationship with PEC performance. The important discoveries enabled by this multi-technique combinatorial study include: (i) a new high-performing combination of Mo and Gd incorporated as alloying metals, which would not have been found *via* a gradient search technique for improved performance; (ii) Mo and Gd alloying separately and together introduce variation in the monoclinic distortion with select stoichiometries producing a substantial deviation from Vegard-like linear trends; and (iii) the anomalously high PEC performance of select (Mo,Gd) co-alloyed compositions is well described by improvements to carrier lifetime and/or transport that result from the higher crystal symmetry when the monoclinic distortion is lowered.[10]

While our study focuses on the monoclinic (distorted scheelite) $BiVO_4$ (m-$BiVO_4$) and continuous deformations of this structure, we note that the related tetragonal scheelite (t-$BiVO_4$) has also been studied. Despite the close structural relationship and band gap energies of m-$BiVO_4$ (2.41 eV) and t-$BiVO_4$ (2.34 eV), comparison of photocatalytic activity in the presence of a sacrificial electron acceptor (silver nitrate) indicated that the room-temperature stable m-$BiVO_4$ is more photoactive than the metastable t-$BiVO_4$, although key properties such as grain size and crystallinity were quite different between the compared samples due to the synthesis of m-$BiVO_4$ through gradual dissolution and precipitation starting from a t-$BiVO_4$ powder.[11] The tetragonal zircon phase (z-$BiVO_4$) is undesirable due to poor performance and a substantially higher band gap of 2.9 eV.[12] ‡

Doping, or low level alloying of three, four, or more additional metals into m-$BiVO_4$ is an active area of research, with particularly notable performance enhancements achieved by inclusion of Mo, W, and select rare earth elements, alone and in combination.[13–19] The underlying origin of the observed performance improvement remains an active area of investigation, with spectroscopic studies indicating a decrease in electron trap state concentration producing an increase in electron and hole mobilities[10] and/or increased charge carrier concentration induced by electron donating elements, in particular W and Mo.[20] Changes in the band gap and movement of band edges have also been reported.[21]

Several combinatorial studies have contributed to this broad m-$BiVO_4$ alloying effort through systematic variation of alloy concentration using wet chemical synthesis or physical vapor deposition techniques. Park *et al.*[22] fabricated a discrete composition array of W and/or Mo alloys of the form $Bi_{0.5}V_{0.5}$:W$_x$Mo$_y$[23] with both x and y ranging from 0 to 10% at 2% intervals. The photocurrent for sulfite oxidation in aqueous electrolyte was maximized at all applied potentials with the $Bi_{0.5}V_{0.5}$:W$_{0.02}$Mo$_{0.06}$ composition, indicating a synergistic effect from co-alloying of W and Mo. Another 12 elements were alloyed with W but offered no improvement with respect to the best W-based alloy. Supported by computation, a primary conclusion drawn from this work is that Mo and W alloying, separately and together, serve as shallow electron donors. Later work by Jiang *et al.*[14] used ink jet printing to produce discrete composition arrays to compare the effect of alloying each of W, Mo, Mn, Co, Cr, Mg, Fe, Cu. Measurements in 0.1 K_2SO_4 revealed that the best PEC performance is obtained with W alloying.

Physical vapor deposition has been employed for optimization of Mo and/or W alloying into m-$BiVO_4$,[24,25] and more recent work by Gutkowski *et al.*[15] has explored a larger range of composition through synthesis of thin film metal oxides Bi(V–Mo–B)O_4 (B = Ta, W, Nb). XRD and Raman characterization of the phase behaviour revealed that the isovalent V substituent (Nb or Ta) can co-alloy into m-$BiVO_4$ along with the electron donor substituent (Mo). While excellent PEC performance was obtained with the (Mo,Ta) and (Mo,Nb) alloy systems in 0.1 M $Na_2B_4O_7$ electrolyte (pH 9),

---

‡ International Center for Diffraction Data (ICDD) entries 01-083-1699 (m-$BiVO_4$), 01-075-2481 (t-$BiVO_4$), 00-014-0133 (z-$BiVO_4$).

the (Mo,W) system provided the best overall performance. While these works collectively signify the opportunities for performance optimization *via* alloying, challenges remain to effectively identify co-alloying combinations that induce improvements beyond those resulting from (Mo,W)-based electron donation. We address these challenges using combinatorial and high throughput techniques, ultimately revealing that carrier transport can be improved by tuning the monoclinic distortion with co-alloying.

Experimental

Library design and synthesis

The design of a composition library to explore any type of alloying poses several challenges. Given prior knowledge about the type of alloying, *i.e.* interstitial or substitutional on 1 or both sites, a composition library can be designed accordingly. For example $(Bi_{1-0.5n}Na_{0.5n})(V_{1-n}Mo_n)O_4$ is a specific co-alloying design wherein substitutions of Na^{1+} on the Bi^{3+} site and of Mo^{6+} on the V^{5+} site provide n-invariant charge balance assuming a constant O stoichiometry.[26] To more generally explore alloying space, including the possible variation of O stoichiometry and any combination of interstitial and substitutional alloying, we designed a composition library that covers a range of alloy loading for each of 6 elements, and a range of both composition and loading for each pairwise combination (6-choose-2 = 15) of the alloying elements. The fabrication of this composition library on a single library plate facilitates establishment of composition-property trends with minimal convoluting factors.

The composition space for alloying cations A and B into $BiVO_4$ is the Bi–V–A–B composition space containing 3 compositional degrees of freedom, which we parameterize as $Bi_{1-x}V_x:(A_{1-z}B_z)_y$ where x is V/(Bi + V) for the "base" material into which alloys are added; y is the loading of the alloying elements, (A + B)/(Bi + V); and z is the alloy composition B/(A + B)

when 2 alloying elements are present. For a single alloying element, this reduces to $Bi_{1-x}V_x:A_y$. If, for example, the element A substitutes onto only the V site or only the Bi site, the stoichiometry of the 2 lattice sites is maintained if $x = 0.5 - y/2$ or $x = 0.5 + y/2$, respectively.

Our composition library was designed to combinatorially vary each of x, y and z while keeping the other 2 composition variables constant, for example by varying y from 0% to approximately 8% with select, constant values of x and z. To attain the site-balanced stoichiometry for single-site-alloying about half way along this composition gradient, Bi–V compositions of $x = 0.48$ and $x = 0.52$ were included in the library, in addition to $x = 0.5$. For each of these 3 values of x, the $y = 0$ "base" (no alloying elements) compositions were included along with 10 values of y for each alloying element A and 17 compositions (combinations of $y > 0$ and $0 < z < 1$) in each of the 15 Bi–V–A–B composition spaces, making the total number of unique compositions

$$3 + (3 \times 10 \times 6) + (3 \times 17 \times 15) = 948, \qquad (1)$$

where the three terms in the sum correspond to the alloy-free "base" compositions, single-alloy compositions, and co-alloy compositions, respectively. In addition, 16 duplicates of each base composition and 5 duplicates of each single-alloy composition bring the total number of photoanode samples to 1713. A portion of the layout showing 3 duplicates of the 3 base compositions and 1 duplicate of each Bi–V–A composition set is shown in Fig. 1a. This "systematic" layout of the compositions enables rapid visual inspection of printing quality, and the additional duplicates of each of these compositions are intermixed with the Bi–V–A–B compositions with randomization of the compositions within the grid of sample locations, as further described in the ESI.†

All samples were prepared on a single library plate, 100 × 150 × 2.2 mm soda lime glass with TEC-15 SnO_2:F coating, (Hartford Glass) by inkjet printing (Microfab Technologies JetLab4).
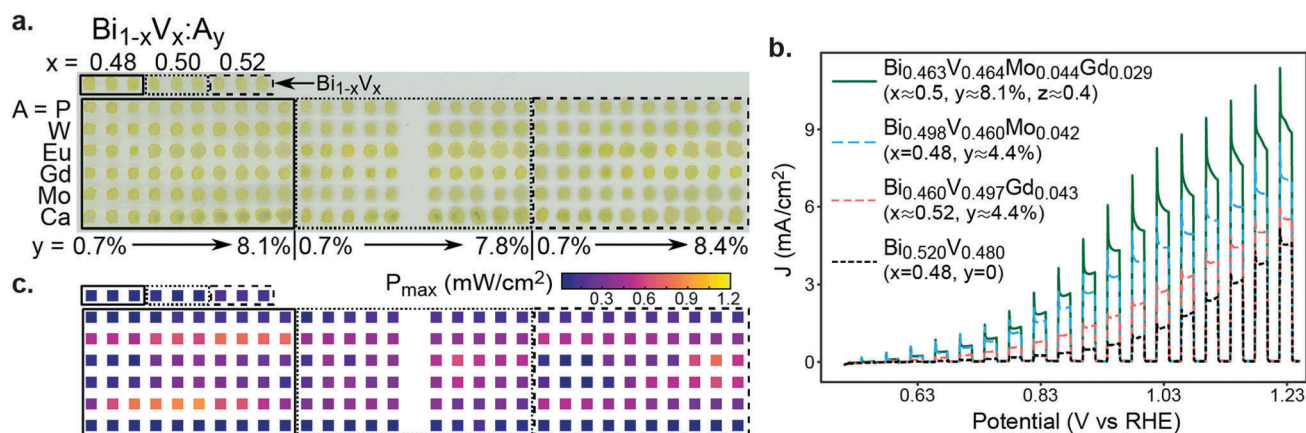

Fig. 1 (a) Image of substrate region containing 189 of the 1713 samples in the photoanode library, including 3 different Bi–V stoichiometries (x) for 10 different alloying concentrations (y) and for each of 6 alloying elements (A). The non-pictured portion of the library contains four duplicates of each of these composition samples, which are intermixed with dual alloying compositions for the 15 pairwise combinations of the 6 alloying elements. (b) The anodic sweep of a chopped-illumination CV is shown for 4 samples with each composition labeled first as a normalized composition (excluding oxygen) and then as x, y, z coordinates in the parameterization of the alloying space. (c) Automated processing of each anodic sweep produces the maximum photoelectrochemical power generation (P_{max}), which is mapped for the samples shown in (a).

The "inks" contained elemental precursors with each composition sample created through controlled mixing of up to 128 drops from 1 to 4 of the 8 inks, each containing 15 vol% diethylene glycol and 1 or 2 of the following metal precursors: $Bi(NO_3)_3\cdot5H_2O$, $VOSO_4\cdot5H_2O$, $(NH_4)_3PO_4$, $(NH_4)_{10}(H_2W_{12}O_{42})\cdot4H_2O$, $Eu(NO_3)_3\cdot5H_2O$, $Gd(NO_3)_3\cdot6H_2O$, $(NH_4)_6Mo_7O_{24}\cdot4H_2O$, and $Ca(NO_3)_2\cdot4H_2O$. One Bi–V ink was prepared containing 0.156 M Bi and 0.144 M V to create the $x = 0.48$ composition and a second ink with 0.11 M V was used to increase the value of x. The remaining 6 inks were prepared with 0.022 M of the respective alloying elements. Additional variations in sample printing were introduced to mitigate covariance among sample properties such as metal loading of the samples. Due to the granularity of the ink stoichiometry, many of the target compositions are printed "approximately" with less than 1 atom% deviations. For presenting results, all compositions are labelled according to their intended cation composition and approximate x, y, z values are used. For example, $y \approx 1.5\%$ represents loadings of 1.5%, 1.4% and 1.5% for $x = 0.48$, 0.5 and 0.52, respectively. Similarly for $y \approx 2.9\%$, 4.4%, and 8.1%, the triplets of loadings for the 3 respective values of x are 2.9%, 2.8%, 3.0%; 4.4%, 4.2%, 4.5%; and 8.1%, 7.8%, 8.4%. Following inkjet deposition, the samples were dried in a 35 °C oven and calcined at 565 °C in pure O_2 for 30 min. Scale up of select compositions was achieved by spin coating a solution containing the same elemental precursors used for inkjet printing, as further described in the ESI.†

Photoelectrochemistry

PEC characterization of each library sample was performed using a custom scanning drop electrochemical cell (SDC) with integrated front-side illumination, which is an automated system for performing serial PEC measurements.[27] A Pt counter electrode and Ag/AgCl reference electrode were used for 3-electrode cell measurements where the electrochemical potential (E) of the working electrode (library sample) was controlled with a Gamry G 300 potentiostat. Custom software with translation stages sequentially addressed the library samples. Experiments were performed in aqueous electrolyte with potassium phosphate buffer (50 mM each of monobasic and dibasic phosphate) with 0.25 M sodium sulfate as a supporting electrolyte (pH 6.7).

A cyclic voltammogram (CV) was acquired for each sample, which started and ended at 1.26 V vs. RHE and extended down to 0.51 V vs. RHE at 0.02 V s^{-1} with toggling of illumination from a 455 nm light emitting diode (LED, Thorlabs M455F1) using repeated cycles of 1 s off and 1 s on. To avoid prevalence of the current transients upon illumination toggling in the PEC results, the illuminated and dark currents were calculated as the average current over the latter half of the light-on and light-off duration, respectively. The photocurrent was calculated as the difference between each averaged illuminated current and the linear interpolation of the neighboring averaged dark currents, providing a measurement of photocurrent at 0.04 V intervals as described in further detail in ref. 28. Illumination was provided via fiber optic terminated approximately 1 mm

above the library plate, resulting in a 0.86 mm-diameter illumination spot and providing PEC characterization of the corresponding area fraction of the printed samples. This illumination under-filling makes the PEC characterization insensitive to variations in the shape of the sample perimeter. LED power was measured using a Newport 1918-R power meter and Newport 818-UV photodetector, yielding an irradiance of approximately 400 mW cm^{-2}, and the photocurrent values were scaled by the illumination area to obtain the photocurrent density, J_{photo}.

The anodic sweep of the CV was analyzed to determine the photoelectrochemical power generation by fitting the illumination data to a 4-parameter sigmoid function, which was heuristically determined to provide sufficient modelling of the J_{photo}–E signal for each sample. The photoelectrochemical power density of O_2 evolution is taken as the product of J_{photo} and the respective electrochemical potential below the OER Nernstian potential (1.23 V), which is readily calculated from the sigmoid function to determine the maximum photoelectrochemical power generation (P_{max}) for each sample. This calculation assumes that the measured photocurrent is due to the OER, but as long as the OER Faradaic efficiency does not vary with composition, the observed trends in P_{max} and identification of optimal alloys are unaffected by this assumption. The photocurrent density at the Nernstian potential, J_{O_2/H_2O}, was calculated by evaluating the fit function at 1.23 V vs. RHE.

For the base Bi–V compositions and Bi–V–A compositions, the P_{max} value is taken as the median value of the sample replicates, and further statistical evaluation of the measurements on replicate samples indicates that when $P_{max} > 0.5$ mW cm^{-2} the relative error of each P_{max} value is 13%, which has contributions from variation in the high throughput PEC cell and in printed sample morphology. A benefit of the combinatorial PEC measurements is the ability to draw conclusions from compositions trends assembled from numerous PEC measurements with low effective uncertainty.

The AM 1.5G measurements on scaled-up samples were performed in a standard H-cell using a three-electrode configuration at room temperature with Pt counter and 3 M Ag/AgCl reference electrodes. The electrolyte solution contained 0.25 M K_2HPO_4 and 0.25 M KH_2PO_4 (pH = 7.2) with 1 M Na_2SO_3 as a hole scavenger to mitigate photoanodic catalytic barriers presented by water oxidation. Simulated AM 1.5G solar illumination was provided by a Solar Light solar simulator (16S-300-002 V4.0 Air Mass 1.5 simulator) with a flux of 100 mW cm^{-2}, as determined using a calibrated Newport Si PV module. The current vs. voltage characteristics were measured using a Biologic SP-300 potentiostat at a sweep rate of 50 mV s^{-1} from the open circuit voltage to 0.8 V vs. reference first in the dark then under continuous front illumination.

Materials characterization

Validation of the inkjet printing was performed by measuring the molar loading of both V and Bi using X-ray fluorescence (XRF). The 6 alloying elements did not provide large enough XRF signal to enable meaningful confirmation of alloy loadings.

Three replicate Bi–V samples for each value of x were measured and averaged to provide molar loadings of both V and Bi from which the composition and thickness were calculated assuming the bulk m-BiVO$_4$ density of 6.94 g cm^{-3}. The molar loadings were determined using elemental thin film standards to calibrate the intensity of the Bi L and V K XRF peaks. The thin film standards contained 0.084 and 0.34 μmol cm^{-2} of Bi and V, respectively, which are similar to the approximate elemental loadings of 0.12 μmol cm^{-2} in the library samples. While XRF provides excellent sensitivity to composition changes and confirms the intended variation of Bi–V composition, due to possible matrix and thickness effects in the XRF measurements, we estimate the relative uncertainty of the XRF measurements to be 10%.

Optical characterization was performed using a custom built ultraviolet-visible (UV-vis) spectrometer that collects transmittance and total reflectance spectra using a dual integrating sphere assembly fiber-coupled to UV-vis spectrometers (SM303, Spectral Products Inc.), as described previously.[29] Automated data processing to calculate the direct-allowed Tauc signal was recently described in detail.[30]

Structural characterization of select compositions was performed via Raman spectroscopy (Renishaw inVia Reflex) and X-ray diffraction (XRD, Bruker DISCOVER D8). The Raman measurements employed a 20× objective to obtain strong optical coupling to the thin films, resulting in an effective measurement area of approximately 75 μm × 75 μm and motivating the use of the Renishaw Streamline™ imaging capability to acquire about 250 Raman measurements for each composition sample, which were averaged to obtain the representative pattern for the sample. The XRD measurements used a 0.5 mm collimator on Bruker IμS source (Cu Kα) to acquire diffraction signal on about 0.5 mm × 1 mm sample region with the VÅNTEC-500 detector followed by integration into one-dimensional patterns using DIFFRAC.SUITE™ EVA software.

First-principles calculations

To understand the effect of the monoclinic distortion in the electronic and transport properties of BiVO$_4$, we perform first principles density functional theory (DFT) calculations with a plane-wave basis using VASP.[31,32] We use the Heyd–Scuseria–Ernzerhof (HSE) hybrid exchange–correlation functional,[33] where a fraction α of the generalized gradient approximation (GGA)[34] exchange is replaced with exact Fock exchange at short range, and the long-range exchange interaction is screened with a range separation parameter of 0.2 Å^{-1}. Recent DFT calculations have demonstrated that the known monoclinic ground-state structure of BiVO$_4$ is only correctly predicted by DFT with hybrid functionals for larger-than-typical values of α;[35] following this work, we use α = 0.5 in our structural relaxations, which are performed using the conventional unit cell (4 formula units). All relaxations proceed until Hellmann–Feynman forces are smaller than 1 meV Å^{-1}. Our DFT-HSE calculations use a plane-wave energy cut-off of 450 eV, a 4 × 4 × 2 Monkhorst–Pack[36] k-point grid, and projected augmented pseudopotentials with 5, 5 and 6 valence electrons for Bi, V and O, respectively, from the

VASP library.[37] Band structure calculations are generated with the primitive unit cell (2 formula units) of the relaxed structures within the GGA.

Electron and hole polaron formation energies are calculated using spin-polarized DFT with the HSE functional, again with α = 0.5.[38,39] Our polaron calculations use a 2 × 2 × 1 supercell (16 formula units), an energy cut-off of 400 eV and a 1 × 1 × 1 Γ-centered k-point grid. We model a localized electron (hole) polaron by adding (removing) one electron and introducing a compensating background in the supercell, breaking symmetry locally by hand via a small expansion (contraction) of the V–O (Bi–O) bonds at the polaron site, and fully relaxing the structure. To compute the polaron formation energy, we also perform a reference calculation in which we add (remove) a fraction of charge, 1/8 of the electronic charge, in the primitive unit cell containing one formula unit, followed by full relaxation of the unperturbed structure. As mentioned above, in both the polaron and reference calculations, we ensure charge neutrality by adding a compensating uniform positive (negative) charge background. Supercell structures are fully relaxed until Hellmann–Feynman forces are smaller than 0.035 eV Å^{-1}.

Results and discussion

Photoelectrochemical mapping of combinatorial alloy library

An image of part of the alloy composition library is shown in Fig. 1a. Composition samples are parameterized by the alloying elements A, B and composition coordinates x, y, z, where the composition is Bi$_{1-x}$V$_x$:A$_y$ for single-alloy composition spaces and Bi$_{1-x}$V$_x$:(A$_{1-z}$B$_z$)$_y$ for co-alloying composition spaces. For x = 0.48, 0.5, and 0.52 samples, the corresponding values measured by XRF were 0.47, 0.49 and 0.51, respectively. Since these are well within the XRF uncertainty, we continue to label materials according to their intended printed composition. The XRF results also indicate that the equivalent dense-thin-film thickness of the samples is approximately 50–60 nm, which is the most relevant length scale for performing thin film studies. The carrier diffusion length of BiVO$_4$ thin films has been measured to be 70 nm,[40] and optimized photoanodes achieve efficient collection of photogenerated carriers via nanostructuring on this length scale.[3,7,41] By keeping the thin film thickness in this range, we are most sensitive to changes in carrier mobility introduced by the dopants, in particular hole transport, which remains a challenge in BiVO$_4$ optimization as discussed further below.

The PEC experiments were performed using the 2.75 eV illumination (0.15 eV full-width-half-max) source to provide above-gap excitation of the m-BiVO$_4$ materials. With this illumination, trends in PEC performance are primarily due to charge separation and transport effects, particularly in the absence of any blue-shifting of the band edge. The optical measurements made on each sample were used to evaluate changes in band gap energy with alloying composition, and as discussed below no such band edge shifts were observed. The anodic sweep of the CV is shown in Fig. 1b for representative Bi–V, Bi–V–A and

Bi–V–A–B compositions. The observed current transients upon illumination toggling are indicative of substantial surface recombination. Since passivation of surface defects and incorporation of co-catalysts mitigate this surface recombination,[42,43] we focus in the present work on the quasi-steady state photocurrent observed after the sharp transients, which is more indicative of the bulk material properties that are amenable to optimization *via* alloying. While the illuminated open circuit voltage can be estimated from the CV data, the corresponding uncertainty in the composition trends would be high because the alloying-dependent photocurrent alters the detectability of photocurrent at lower potentials, and we do not attempt to disambiguate improvement in photocurrent above the detectability limit with possible shifts in the flat band potential. Instead, we use a primary figure of merit that combines the photocurrent and photovoltage performance, namely the maximum photoelectrochemical power generation for the OER (P_{max}). The P_{max} values for the portion of the library shown in Fig. 1a are shown in Fig. 1c, and exhibit smooth variation in P_{max} with respect to alloy loading for all 3 base compositions and 6 alloying elements.

The span of 15 pseudo-ternary compositions spaces in the 948 unique compositions poses substantial challenges for visualization of PEC and other results, prompting our development of several custom visualizations starting with Fig. 2. Fig. 2a shows the composition maps of P_{max} for all Bi–V and Bi–V–A compositions and 6 of the 15 Bi–V–A–B composition spaces. The analogous mapping of $J_{O2/H2O}$, the photocurrent

density at 1.23 V *vs.* RHE, is shown in Fig. 2b. While there are notable differences in the composition trends of P_{max} and J_{O_2/H_2O}, which indicates that alloying alters the shape of the J_{photo}–E curve, these figures clearly identify Bi–V–Mo and Bi–V–W with $x = 0.48$ and Bi–V–Eu with $x \approx 0.52$ as the top performing alloys in the Bi–V–A composition spaces. The Bi–V–A–B compositions that provide the highest P_{max} values are noted in Fig. 2a and reside in the Bi–V–Mo–Gd space with $x \approx 0.5$. An alternate visualization of P_{max} trends in this composition space (including Bi–V–Mo and Bi–V–Gd) is provided in Fig. 2d, which nicely illustrates that the best performance is observed with Bi–V–Mo–Gd compositions.

The identification of maximum performance in the 4-cation space motivates further inspection of "synergy" of different alloying elements. If A and B contribute to PEC performance through different mechanisms, alloying with both elements may yield superposition of the improvements to attain higher P_{max} values. The element B may also indirectly improve P_{max} by altering materials properties from film morphology to increased solubility of A *via* size compensation, as has been previously observed in functional metal oxides.[44] To further inspect composition trends and identify any such benefits of co-alloying Mo with B = Eu, W, Ca, P, or Gd, Fig. 3 provides an additional visualization of the P_{max} data with all Bi–V–A compositions shown in Fig. 3a and all Bi–V–Mo–B compositions shown in Fig. 3b.

At $x = 0.48$, P_{max} remains in the 0.9–1 mW cm^{-2} range for Mo loading of $0.7\% \leq y \leq 4.4\%$. In Bi–V–A spaces, this performance
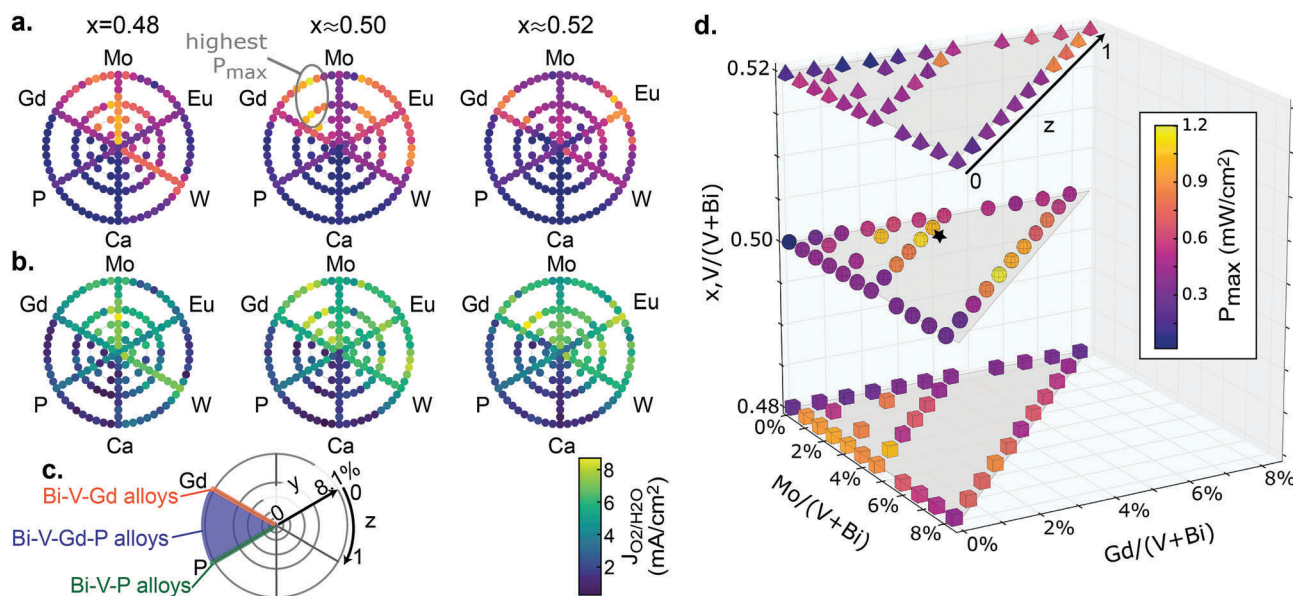

Fig. 2 (a) P_{max} values for 489 of the 948 unique compositions in the photoanode library. In this series of radial plots for each x value, the $Bi_{1-x}V_x$ composition is at the center with the 6 radial lines corresponding to Bi–V–A alloys and the 6 sectors containing Bi–V–A–B alloys. The 9 Bi–V–A–B composition spaces not represented in the 6-sector plots comprise the remainder of the library compositions. (b) The analogous map of J_{O_2/H_2O} values from the same anodic sweep dataset, which upon comparison with the P_{max} map reveals somewhat different compositional trends and indicates the importance of specifying a figure of merit to identify an optimal alloy. (c) Legend for the radial plots in (a and b) showing the radial alloy loading (y) and azimuthal alloy-composition (z) variables. (d) The Mo–Gd sectors from a. are plotted in Cartesian space where the three x values correspond to the 3 highlighted planes, and the black star denotes the Bi–V–Mo–Gd composition used for scale-up studies. The P_{max} color scale is the same for (a) and (d) and is also the same as Fig. 1c.
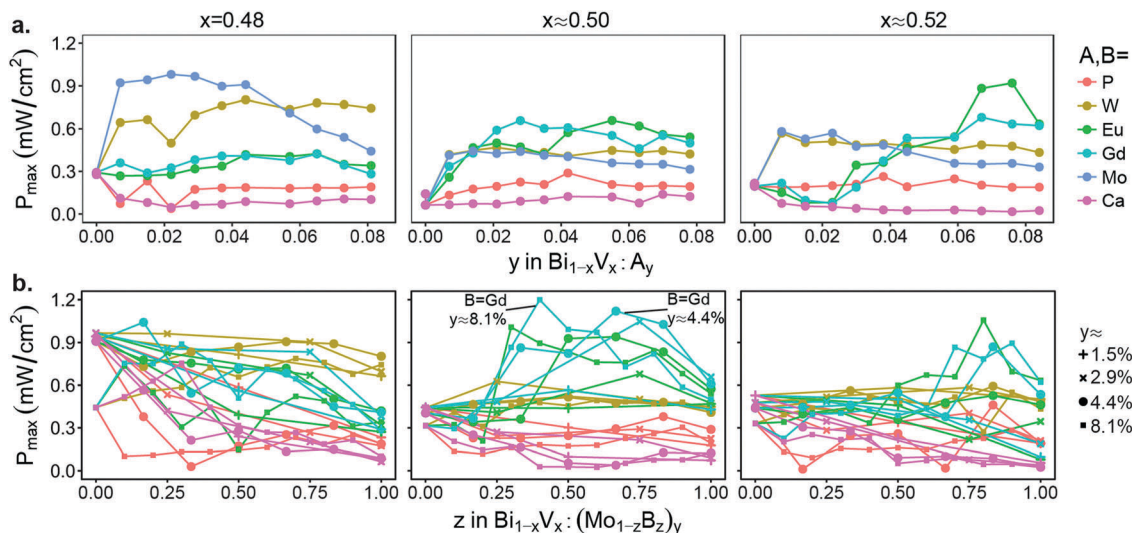
Fig. 3 (a) The P_{max} variation with alloy loading for each Bi–V–A system reveals Mo and W as the best elements with $x = 0.48$ (Bi-rich) and Gd and Eu with $x = 0.52$ (V-rich) compositions. (b) The co-alloying in Bi–V–Mo–B spaces for 5 values of B, each of which includes 4 different total alloy loadings (y) shown as different symbols. Each segmented line spans Bi–V–Mo ($z = 0$) to Bi–V–B ($z = 1$) at the specified loading, with a linear or convex trends expected for Mo–B combinations that do not improve performance beyond the respective alloying sub-spaces. For Mo–Gd with $x = 0.5$, the trends for all 4 loadings are concave with the 2 labelled curves containing the highest P_{max} values. The relative uncertainty in P_{max} for each data point is estimated to be 13%, and for clarity is not illustrated.

is only rivaled by V-rich films with $y \approx 8.1\%$ loading of Eu. In the Bi–V–Mo–B spaces, each signal connects a Bi–V–Mo ($z = 0$) to a Bi–V–B ($z = 1$) composition, creating a large cluster of lines where addition of B to Bi–V–Mo is typically deleterious to PEC performance. At $x = 0.48$, the Bi–V–Mo–W data indicates that high P_{max} values are maintained across the $Mo_{1-z}W_z$ composition line at all alloy loadings (values of y), but no substantial synergy between these alloying elements is observed. The B = Gd and Eu signals rise above those of the other co-alloys with the most compelling composition trends arising from the Bi–V–Mo–Gd system with $x \approx 0.5$, which correspond to the compositions noted in Fig. 2 as having the highest P_{max} values, in particular higher P_{max} than any of the three-cation compositions. The primary phenomenon observed in the PEC characterization is that alloying of either Mo or Gd improves the PEC performance and specific combinations of Mo and Gd co-alloying offer further improvements.

Scale-up for AM 1.5G measurements

While the primary purpose of the present effort is to identify the underlying materials chemistry that gives rise to the observed performance trends in co-alloying composition spaces, we performed initial scale-up experiments to provide confirmation of the enhanced PEC performance with Mo–Gd alloying. The composition indicated by a star in Fig. 2d has relatively low total alloy concentration and is representative of the synergistic co-alloying of Mo and Gd, prompting our choice of this composition to mitigate the risk of precursor and alloy segregation in the scaled-up film. A film with this composition and a control sample with the same Bi:V ratio but no alloying elements were synthesized and characterized by XRF, UV-vis and PEC under AM 1.5 illumination (Fig. S1 and S2, ESI†). The XRF measurement revealed

that the scaled-up $Bi_{0.476}V_{0.476}Mo_{0.014}Gd_{0.034}O_x$ film contained approximately a 1.9-fold increase in the Bi (and V) loading over the library samples (0.23 μmol cm^{-2} compared to 0.12 μmol cm^{-2}), and the corresponding P_{max} value using a measurement similar to that of Fig. 1 and 2 was a factor of approximately 1.8 higher than that expected from the library measurements (see ESI†), indicating the desired increase in photoactivity with increased loading of the absorber, which is likely due to increased light absorption.

Standard epoxy-encased electrodes with exposed electrode areas of 1.57 and 1.21 cm^2 for the control and Mo–Gd sample, respectively, were fabricated and measured with front-side AM 1.5G illumination. Motivated by the hypothesis that charge transport is the primary mechanism by which Mo–Gd improves photoactivity (see below), the AM 1.5 measurements were performed in the presence of a hole scavenger to mitigate influence of catalysis in this photoanode characterization. The absorption spectrum for each scaled-up sample is shown in Fig. S1 (ESI†) and used to calculate the maximum possible photocurrent given the measured absorption of the samples, which is 2.9 and 3.0 mA cm^{-2} for the control and Mo–Gd sample, respectively (see ESI†). The measured photocurrent densities at 1.23 V *vs.* RHE were 0.94 and 1.51 mA cm^{-2} for the control and Mo–Gd sample, respectively, indicating that the Mo–Gd alloy increased the photon-to-current efficiency from 32% to 50%. The illuminated and dark CVs are shown in Fig. S2 (ESI†) along with the corresponding PEC power density curves. The total charge density passed in the 2 illuminated CV cycles on the Bi–V–Mo–Gd sample is 0.0979 C cm^{-2}, which corresponds to 1.01 μmol cm^{-2} of elemental charge, a 4.6-fold excess for complete corrosion of Bi or V or a >60-fold excess for complete corrosion of the Mo or Gd, demonstrating that photocorrosion

does not substantially contribute to the measured CVs. Scaled-up electrodes were also measured without the hole scavenger (Fig. S2, ESI†), and while all photocurrents are expectedly lower, the relative improvement due to Mo–Gd alloying is even more pronounced. While the results provide some verification of the trends observed in Fig. 2, the scale-up synthesis is far from optimal, and to better understand how to exploit the Mo–Gd co-alloying synergy in optimized photoanodes, we return to investigation of the underlying materials chemistry.

Optical, structural and electrochemical trends

Since the Bi–V–Mo–Gd alloys provide both the most important composition trends and best PEC performance, more detailed

characterization of these alloy compositions was performed *via* high throughput UV-vis, Raman and XRD experiments, with each of these techniques producing 1-D patterns for each library sample. The fitted J_{photo}–E curves from PEC experiments comrpise another 1-D dataset that we combine with optical and structural characterization data in Fig. 4. In this data representation we have identified the 2 portions of both Raman and XRD patterns that provide the most important structural characterization and combined them with the UV-vis and J_{photo}–E signals to generate 6-panel figures where each signal is mapped as a function of Mo-loading, Gd-loading, Gd *vs.* Mo alloying with $y \approx 4.4\%$, and Gd *vs.* Mo alloying with $y \approx 8.1\%$ in Fig. 4b–e, respectively. The false-color plots enable facile
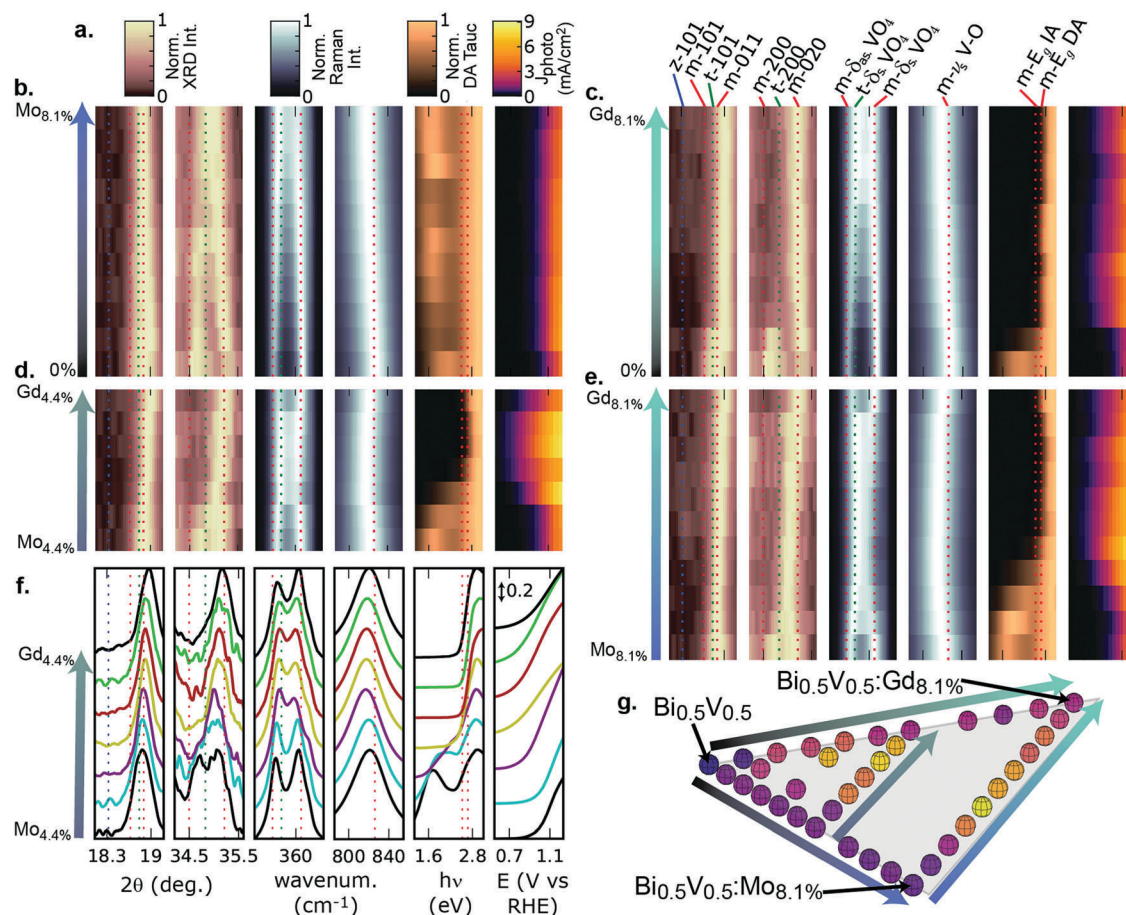

Fig. 4 (a) Combinatorial characterization of Bi–V–Mo–Gd alloys where a. provides the color scale for the normalized XRD, Raman, and UV-vis (Tauc) signals as well as the PEC (J_{photo}) signal; (b–e) contain false color plots for 4 different composition lines; (f) is the stack-plot representations of the data from (d) and also provides the labels for the horizontal axes, where the portions of each signal are chosen to highlight pertinent features; (c) provides the labels for select literature values shown as dashed lines in each respective plot; and (g) provides the visualization of the 4 composition lines, which are all in the $x = 0.5$ plane of Fig. 2d. False color plots shown for all 4 composition lines aid visual recognition of trends among the 4 composition lines. The descriptions of the dashed lines are as follows: z-101 is the {101} XRD peak for the zircon polytype and is a distinguishing peak to confirm that this polytype is not observed in any substantial phase fraction. The tetragonal scheelite ("t") {101} and {200} XRD peaks split to {101} and {011} and to {200} and {020} peaks for the monoclinic (distorted scheelite) phase ("m"). Similarly the VO_4 bending mode (δ_s) in t-$BiVO_4$ splits into asymmetric (δ_{as}) and symmetric (δ_s) modes in m-$BiVO_4$. The alloying-driven lessening of the monoclinic distortion results in merging of each of the monoclinic doublet peaks, and the δ_{as} and δ_s peaks provide the best resolution of the monoclinic distortion and reveal that none of these materials have tetragonal symmetry. The symmetric V–O bending mode (ν_s) is also shown at the value for m-$BiVO_4$. The literature positions of the indirect (IA) and direct (DA) allowed band gaps of m-$BiVO_4$ are shown with each composition showing a strong increase in DA Tauc signal in this energy range and many compositions exhibiting substantial sub-gap absorption that is modulated in both intensity and characteristic photon energy through alloying. Each J_{photo} signal is the fitted curve to the chopped-illumination anodic voltage sweep and as the only non-normalized type of signal in the figure, a 0.2 mA cm^{-2} scale bar is shown in (f).

comparison of signals across these composition spaces, and the data from Fig. 4d is also plotted as a stack plot in Fig. 4e, which provides better visualization of peak shifts. The stack plots from other composition lines are shown in Fig. S3 (ESI†). Pertinent literature values for each type of signal are also shown in each figure and labelled in Fig. 4c to assist in visualization of trends within and among the composition spaces.

This visualization of the J_{photo}–E curves provide particularly striking evidence of the composition-dependent PEC improvements. As shown in Fig. 1b and right-most panel of Fig. 4f, many samples exhibit J_{photo} signals with positive curvature over the entire potential window, which implies a low fill factor (less than 0.25). On the other hand, the top performer $Bi_{0.463}V_{0.464}Mo_{0.044}Gd_{0.029}$ ($x \approx 0.5$, $y \approx 8.1\%$, $z = 0.4$) sample shown in Fig. 1b exhibits negative curvature over a majority of the potential window, which contributes to the high P_{max} value and indicates substantial improvement in the semiconductor quality of this photoanode. In the false color maps in Bi–V–Mo–Gd space (Fig. 4d and e), this type of improvement to the J_{photo}–E curve is evident in the presence of substantial photocurrent (purple to yellow colors) over the majority of the potential window for select Bi–V–Mo–Gd compositions.

To compare optical properties with that of stoichiometric m-$BiVO_4$, literature values for the 2.52 eV indirect allowed (IA) and 2.68 eV direct allowed (DA) band gaps are overlaid on the DA Tauc signals in Fig. 4.[45] The literature UV-vis data also shows substantial sub-gap absorption that decreases monotonically with decreasing photon energy through the visible spectrum,[45] and while a number of the alloy samples exhibit absorption spectra in excellent agreement with this work, others exhibit an additional optical feature that, to the best of our knowledge, is not reported in the literature but may be related to increased subgap absorption observed with Mo-alloying.[46] The DA Tauc patterns of the $x = 0.48$ samples (Fig. S4, ESI†) appear similar to that of ref. 45 with a slightly lower apparent DA gap of 2.45–2.5 eV, which is similar to that observed by UV-vis in other works.[24,47] The patterns for more V-rich samples, for example $x \approx 0.5$ shown as the bottom composition in Fig. 4b and c, contain a strong sub-gap absorption peak near 2 eV, leading to our conjecture that this sub-gap absorption is related to excess V, and to the extent that the sub-gap absorption from Mo alloying is a consequence of its donated electrons, these observations indicate that the V-rich library samples contain a high free electron concentration. This absorption feature varies with alloy composition and concentration, as shown in Fig. 4, where at $x \approx 0.5$, addition of $y \approx 8.1\%$ Mo red-shifts the peak to 1.6 eV whereas the addition of only $y \approx 0.8\%$ Gd appears to blue shift the peak by more than 0.5 eV such that it merges with the band gap absorption edge and no longer appears as a resolved peak. Commensurate shifting of the absorption peak is observed along the Mo–Gd composition lines at both $y \approx 4.4\%$ and 8.1%, and with $x = 0.48$ samples (Fig. S4, ESI†). On average, the photon energy of the subgap absorption peak shifts by about -0.05 eV per atom% of Mo.

Given the dramatic improvement in photoactivity upon addition of Mo, there is no indication that this subgap

absorption is deleterious to the photoanode performance, but it may obscure any small shifts in the DA band edge. So even though band gap tuning is a common objective of alloying studies,[47] we do not map compositional trends of band gap energy in the present work. The Tauc signals for the Bi–V–Mo–Gd samples with highest P_{max} values are shown in Fig. S5 (ESI†), revealing that the direct band gap shifts by no more than 0.1 eV from that of the base $BiVO_4$ sample.

To develop a data-driven hypothesis regarding the origin of the (Mo,Gd) co-alloying synergy, we continue examination of Fig. 4 under consideration of structural properties. Grain size and orientation can play a critical role in photoelectrochemical performance,[7] prompting detailed analysis of the XRD data. Representative XRD images from the area detector are shown in Fig. S6 (ESI†), demonstrating that across these alloy compositions the films are equi-axed (powder-like random orientations), i.e. there is no compositional variation in crystallite orientation. The XRD patterns in Fig. 4 reveal that the XRD peak widths do not appear to vary substantially with alloy composition. To provide a quantitative measure of composition-dependent changes in XRD peak width, which is inversely related to the characteristic grain size, the m-$BiVO_4$ {004} peak was chosen since it has no overlapped peaks, and in particular this c-axis reflection does not involve monoclinic peak splitting. Since the instrument broadening may vary slightly among patterns, the nearby FTO{110} peak from the underlying layer was used as an internal calibrant to monitor crystallite grain size variation with Bi–V–Mo–Gd alloy composition, as shown in Fig. S7 (ESI†). The approximate grain size for all samples is 27 nm (calculated from m-$BiVO_4${004} peaks without consideration of instrument broadening) and increases somewhat systematically with increasing Gd concentration. While this trend is important to note, its lack of correlation with the trends in P_{max} indicate that grain size does not account for the noted synergy of Mo–Gd co-alloying.

In Fig. 4, the systematic variation in Raman signal, and in particular peak positions, across each composition line reveals that the Raman signal does not vary monotonically along the Mo–Gd composition lines. Similar Raman peak shifts have been noted in Mo- and W-alloying in sputter-deposited alloy libraries.[15] To enable quantitative interpretation of the shifts we turn to inspection of alloy and temperature-dependent studies by Zhou et al.[26,48] of $(Bi_{1-0.5n}A_{0.5n})(V_{1-n}Mo_n)O_4$ where A = Li or Na. The temperature of m-$BiVO_4$ to t-$BiVO_4$ phase transition in this system was found to drop precipitously with addition of Mo (increase in n) by approximately 21 K and 25 K for A = Li[48] and Na,[26] respectively, for every 1% of Mo on the V site. These works show very nicely that starting from m-$BiVO_4$, either increasing temperature or increasing alloying lowers the monoclinic distortion continuously and smoothly until the higher-symmetry t-$BiVO_4$ phase is obtained. In Raman characterization, the primary indicator of this monoclinic distortion is the split between the symmetric (s.) and antisymmetric (as.) bending modes of the VO_4^{3-} structural units, for which we adopt the nomenclature $\delta_s(VO_4^{3-})$ and $\delta_{as}(VO_4^{3-})$, respectively.[49,50] For brevity, we use δ_s and δ_{as} to refer to both the respective modes

and their respective peak position in Raman patterns. These bending modes are also referred to as deformation or ν_2 modes, and in the t-BiVO$_4$ phase there is a single mode (single Raman peak).[26,48,51] To quantify how the $\delta_s - \delta_{as}$ Raman peak splitting relates to the monoclinic distortion, which we quantify using the ratio of monoclinic lattice constants (a/b), we use the XRD and Raman data by Zhou *et al.*,[26] which indicates that the relationship is well-described by

$$a/b = 1 + (\delta_s - \delta_{as}) \times 4.82 \times 10^{-4} \text{ cm,} \qquad (2)$$

where the proportionality constant is calculated from the a/b value of 1.020 and ($\delta_s - \delta_{as}$) value of 41.5 cm^{-1} for ambient-temperature, stoichiometric m-BiVO$_4$. From this relationship, the Raman measurement of δ_s and δ_{as} enables distinction between t-BiVO$_4$ and the family of m-BiVO$_4$ with continuously-variable lattice parameters.§ The alloy-dependent monoclinic distortion in m-BiVO$_4$ is also an important consideration for technology deployment as the elevated, varying operating temperature will result in a variable monoclinic distortion.

Starting with the Mo-alloying in Fig. 4b, the trends in XRD and Raman signals are similar to those of ref. 26 with the non-alloy ($y = 0$) patterns matching those of stoichiometric m-BiVO$_4$. With increased Mo content, both the splitting between the (200) and (020) XRD peaks and the splitting between δ_s and δ_{as} Raman peaks smoothly decrease as expected for a slightly reduced monoclinic distortion. More substantial convergence of these split peaks is observed with Gd alloying in Fig. 4c. With the broad peaks from this thin-film XRD data, the peak splitting quickly becomes difficult to resolve, which could lead to the interpretation that the monoclinic distortion has vanished, *i.e.* that the t-BiVO$_4$ phase was formed. However, the splitting of δ_s and δ_{as} remains, demonstrating that for our material and characterization techniques, the Raman experiment is more sensitive to the monoclinic distortion, prompting our analysis of each Raman pattern (see Fig. S8, ESI†) to extract the peak splitting and calculate the monoclinic distortion using eqn (2), resulting in Fig. 5a.

Before continuing with interpretation of Fig. 5, we note that the Raman data also shows a systematic shift in the strongest m-BiVO$_4$ Raman peak, the symmetric V–O stretch (ν_s). The peak shifts to lower wavenumber and broadens with either Mo or Gd alloying, as has been observed previously.[46,52] The peak shift is even more pronounced with Mo and Gd co-alloying. This shift may be indicative of a lowered V–O bond length, which is the interpretation used for Mo^{6+} and W^{6+} substitution onto the V^{5+} site,[15] but our observed shifting of this peak does not directly correlate with Mo concentration, for example along the Mo–Gd co-alloying lines the peak continues to shift downward as the

§ Lowering the monoclinic distortion to a finite value does not constitute a phase change, which has been a point of confusion in the literature with descriptions such as "mixture of monoclinic and tetragonal structure"[10] possibly being interpreted as a 2-phase material when the material is in fact a single monoclinic phase with a distortion between that of room temperature, stoichiometry m-BiVO$_4$ and the null distortion of t-BiVO$_4$. This distinction is critical, especially when monoclinic-split peaks in XRD or Raman begin to merge and can be (erroneously) modelled as a combination of m-BiVO$_4$ and t-BiVO$_4$ reference patterns.[59]
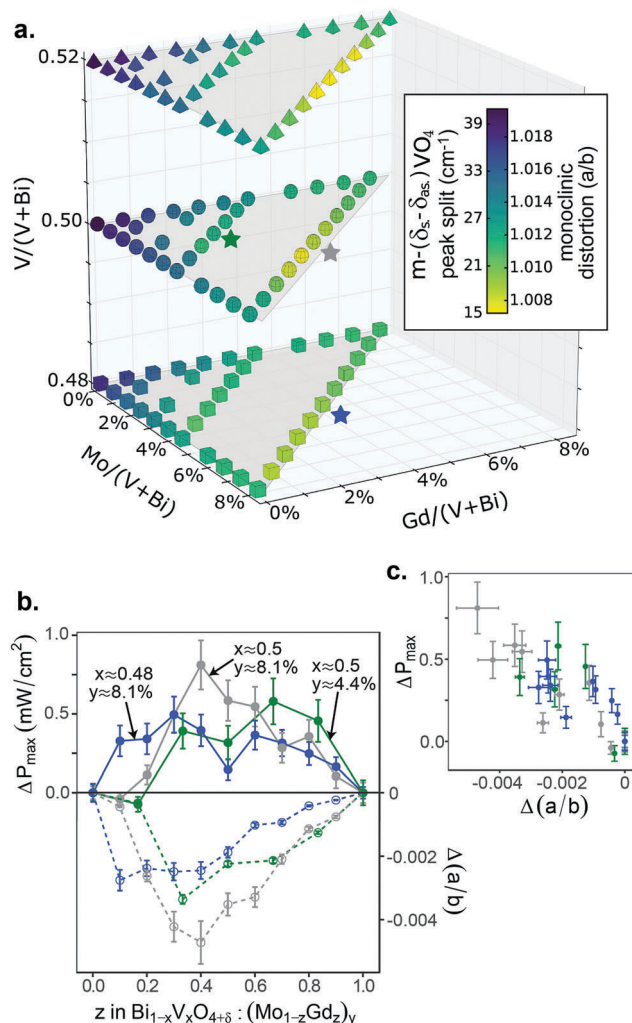

Fig. 5 (a) Map of the level of splitting of the asymmetric (δ_{as}) and symmetric (δ_s) VO$_4$ bending modes from Raman characterization of Bi–V–Mo–Gd alloys. The false color scale is also annotated with the monoclinic distortion inferred from the Raman peak splitting using eqn (2). (b) For the 3 composition lines marked by stars in (a), both P_{max} and monoclinic distortion are plotted as deviations (Δ) from the linear interpolation between the respective endpoint Bi–V–Mo and Bi–V–Gd compositions. (c) The left-y and right-y axis data from (b) are plotted to highlight the strong correlation between the decrease in monoclinic distortion below the Vegard law expectation and the co-alloying enhancement of P_{max}. The Pearson correlation coefficient of these data is −0.83.

concentration of Mo decreases, indicating a different cause for the alteration of this vibrational mode. Hardcastle *et al.*[50] studied a variety of bismuth vanadate phases and noted that increased symmetry within the VO$_4$ tetrahedron also shifts the symmetric V–O stretching mode (ν_s) to lower wavenumber, which is also noted by Gotić *et al.*[49] and observed by Zhou *et al.*[26] The trends in Fig. 4 are commensurate with this phenomenon, with decreases in both ($\delta_s - \delta_{as}$) peak splitting and ν_s peak position resulting from lowered distortion of the VO$_4$ tetrahedron, which is concomitant with lowered monoclinic distortion in the parent crystal structure. Fig. S9 (ESI†) demonstrates that both types of peak shifts that indicate lowered monoclinic distortion

are exhibited by the scaled-up Bi–V–Mo–Gd film used for AM 1.5 measurements.

The composition map of the monoclinic distortion in Fig. 5a, which includes the $x \approx 0.5$ compositions of Fig. 4 as well as the analogous $x = 0.48$ and $x \approx 0.52$ compositions, is remarkably similar to the P_{max} map of Fig. 2d. The simplistic interpretation of this similarity is that lowered monoclinic distortion leads to higher P_{max}, but quantification of this relationship is obfuscated by the co-variant compositional variables. To quantify the level of improvement of the co-alloying over that projected by the Mo- and Gd-alloying data, we invoke a Vegard's law-type analysis and employ linear interpolation in composition space. Considering $Bi_{1-x}V_x$:Mo_y and $Bi_{1-x}V_x$:Gd_y as endpoints of a composition line, interpolation between these endpoints provides a simple model for the expected composition–property relationship. In particular, for structural parameters such as the monoclinic distortion, Vegard's Law suggests that the co-alloy data should follow this linear interpolation. We denote the deviations of co-alloy measurements from this linear interpolation as ΔP_{max} and $\Delta(a/b)$ for P_{max} and monoclinic distortion, respectively. A positive ΔP_{max} indicates co-alloy synergy as discussed with regards to Fig. 3b, and using this model ΔP_{max} was calculated for all 180 co-alloying composition lines (3 values of x and 4 values of y in 15 co-alloying composition spaces). The 3 lines with the highest ΔP_{max} values (which happen to not be the 3 lines with highest P_{max} values) are all Mo–Gd co-alloying composition lines, specifically $x \approx 0.5$, $y \approx 8.1\%$; $x \approx 0.5$, $y \approx 4.4\%$; and $x = 0.48$, $y \approx 8.1\%$. The ΔP_{max} and $\Delta(a/b)$ signals for these 3 composition lines are shown in Fig. 5b, revealing that any composition exhibiting an anomalously high P_{max} value also exhibits an anomalously low monoclinic distortion. This anti-correlation is explicitly shown with the condensed data representation of Fig. 5c and corresponding Pearson correlation coefficient of -0.83.

The XRD data is not sufficient to resolve the monoclinic peak splitting and perform structural refinement, but we note that the centroids of the {101} and {200} peaks in the XRD signals of Fig. 4 vary monotonically across the Mo–Gd alloying space, indicating that Mo and to a lesser extent Gd alloying expand the m-$BiVO_4$ lattice according to the expectation of Vegard's law. More generally, no other observed parameter from structural or optical characterization correlates with ΔP_{max}, the co-alloying performance enhancement beyond that expected from the single alloys, the way $\Delta(a/b)$ does, demonstrating that the monoclinic distortion is a key parameter for PEC performance. To explore the underpinnings of the improvement to PEC performance with lowered monoclinic distortion, we consider bulk properties such as charge separation and carrier transport that may benefit from this structural alteration.

Structural effects of Gd, Mo or W substitutions in m-$BiVO_4$

While alloying elements such as Mo and W primarily improve performance by providing charge carriers,[20,53,54] hole transport remains critical for PEC performance. Pattengale et al.[10] recently revealed through transient absorption spectroscopy that W alloying alters hole traps and thereby improves carrier

lifetimes with lowered recombination rates. The authors additionally asserted that the reduced monoclinic distortion in these alloyed materials may contribute to the mitigation of hole trapping due to the increased symmetry in the local structure of Bi sites. In the ESI,† we present first-principles calculations verifying a reduction of monoclinic distortion with alloying. Table S6 (ESI†) reports Bi–O bond lengths for monoclinic $BiVO_4$ as well as for supercells with substitutional defects where 1 out of the 16 equivalent lattice sites has been replaced with the respective alloying element. The single substitutional defects we consider in our supercells include Gd on the Bi site, Mo on the V site, and W on the V site. All 3 types of substitution lower bond length asymmetry, which is concurrent with a reduction in the monoclinic distortion. We also consider the combination of Mo and Gd substitutions, which results in a more pronounced increase in symmetry compared to the independent Gd or Mo substitutions, demonstrating the important structural influence of Gd–Mo co-alloying.

To the extent that the Pattengale et al.[10] assertion that the removal of hole trap states is continuously improved with lowering of the monoclinic distortion, this phenomenon may contribute to our observed trends in the Mo–Gd alloying space, in particular Fig. 5b. While the study of the W-alloys of ref. 10 and the (Mo,Gd) alloys of the present work involve decreased but not eliminated monoclinic distortion, the finding that a diminsihed monoclinic distortion improves PEC performance is contrary to the report that t-$BiVO_4$ is relatively inactive.[11] While an optimal monoclinic distortion between m-$BiVO_4$ and t-$BiVO_4$ may exist, the photocatalytic activity of t-$BiVO_4$ has only been assessed in the literature using a coarse powder sample,[11] motivating more detailed investigation of $BiVO_4$ thin films with small to zero monoclinic distortion.

Understanding distortion-dependent charge transport

To explore other possible improvements that may arise from co-alloying and in particular a reduced monoclinic distortion, we turn again to first principles calculations. As described in the ESI,† while the effect of dilute Mo and Gd substitutions on the m-$BiVO_4$ electronic structure can be simulated through DFT calculations of large supercells containing single and combined defects, the need for hybrid functionals or a higher level of theory to determine trends in the structural and electronic properties of m-$BiVO_4$ makes these calculations prohibitively expensive for systems that are any more realistic than the supercells we describe above and in the ESI.† Given the strong correlation between improved performance and a lowering of the monoclinic distortion evident in Fig. 5, we focus our structure-dependent electronic structure calculations on stoichiometric m-$BiVO_4$ by varying its monoclinic angle systematically and computing the resulting electronic structure for the series of $BiVO_4$ structures. We start by performing a full structural relaxation of both m-$BiVO_4$ and t-$BiVO_4$ using HSE with $\alpha = 0.5$, yielding lattice parameters (Table S1, ESI†) in excellent agreement with experimental values, including a monoclinic ratio of $a/b = 1.02$ in the fully relaxed m-$BiVO_4$ structure.[55] (In our calculations, the t-$BiVO_4$ phase lies 4 meV per formula unit above m-$BiVO_4$.)

We then interpolate between these structures and extrapolate to higher monoclinic distortion by varying the lattice parameters and atomic positions linearly, as detailed in the ESI.†

Our first-principles DFT calculations of the band structure for fixed monoclinic angle are all within the GGA. We use the primitive unit cell, and generate band structures for the tetragonal structure and 6 additional structures with increasing monoclinic distortion. The results are shown in Fig. 6 and they are in good qualitative agreement with previous calculations.[56–58] The conduction band displays several nearly degenerate local minima dominated by localized V 3d states, whereas the valence band is dominated by hybridized Bi 6s and O 2p states. Along high symmetry paths, the band gap is between points along the Γ–V line and the Z point. For t-BiVO$_4$, we predict a direct band gap approximately 0.1 eV lower than that of m-BiVO$_4$, and since the Mo–Gd alloying (Fig. 4) leads to a structure between that of these two phases, the small change in direct band gap may not be detectable by UV-vis experiments. Aligning the deep oxygen 1s core states of these two structures in our calculations reveals that the VBM of t-BiVO$_4$ is approximately 0.03 eV higher

(closer to vacuum) than that of m-BiVO$_4$, indicating that the monoclinic distortion does not lead to substantial variation in the alignment of VBM with the OER Nernstian potential.

With no substantial variation in band energetics with monoclinic distortion we turn to an examination of transport properties, in particular calculations of the hole effective mass and polaron formation energy. Fig. 6b shows the calculated DFT-GGA hole effective mass as a function of monoclinic distortion, revealing an 18% increase from t-BiVO$_4$ to m-BiVO$_4$. From the perspective of monoclinic distortion, the lower distortion afforded by (Mo,Gd) co-alloying reduces the hole mass by about 10%, a significant improvement consistent with the trend in improved efficiency observed with co-alloying.

Our calculations of the structures and formation energies of localized hole polarons, quasiparticles formed by a hole and an accompanying lattice distortion, indicate that a localized polaron features a local deformation of the BiO$_8$ cage and a 6% average contraction of the Bi–O bonds for m-BiVO$_4$, in agreement with previous DFT results.[39] The hole polaron formation energy, computed from DFT-HSE as described earlier in the manuscript, is 3% larger for m-BiVO$_4$ compared to t-BiVO$_4$ (see Table S3, ESI†), indicating increased hole polaron stabilization and thus less band-like transport in m-BiVO$_4$. This modest difference in hole polaron energy would not be sufficient to constitute a change from polaron-like to band-like hole transport as the monoclinic distortion changes, contrary to prior conclusions that hole conduction is polaron-like and band-like in t-BiVO$_4$ and m-BiVO$_4$, respectively.[39] As noted above regarding experimental comparison of these phases and reiterated here in terms of the first principles calculation of their transport properties, the published literature does not sufficiently distinguish m-BiVO$_4$ as a better photoanode material than t-BiVO$_4$, and our experimental and computational results indicate that opposite may be true.

Our first principles calculations indicate that the improvement in hole effective mass with lowered monoclinic distortion provides the clearest explanation for the measured trend in Fig. 5. Given that these hole transport improvements are distinct from the effects of electron donation noted in many BiVO$_4$ alloying studies, we conclude that the alloying-based PEC improvement originates from a combination of (i) the well-known increase in electronic conductivity with Mo and/or W alloying and (ii) a hole transport-enhancing lowering of the monoclinic distortion that is identified by the present work and is most prevalent once electronic conductivity is no longer limiting performance.
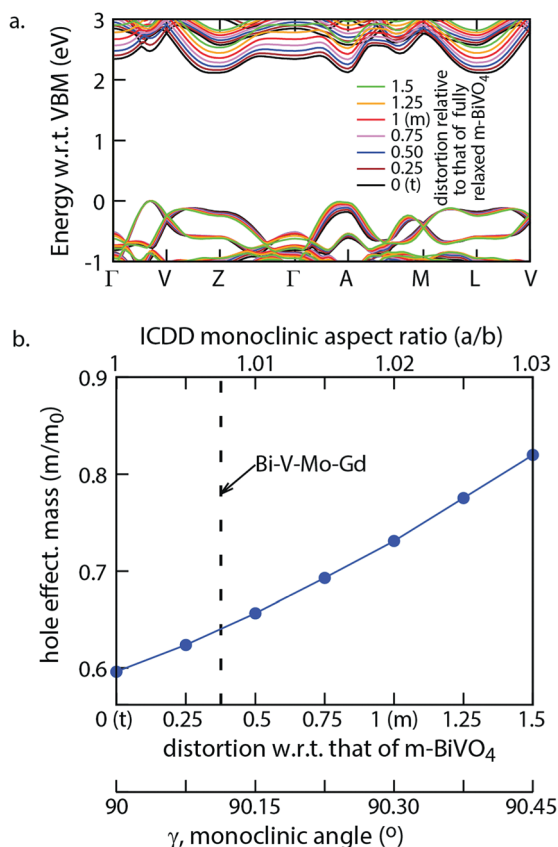

Fig. 6 (a) Computed band structure (DFT-GGA) for a series of crystal structures including the high-symmetry, DFT-HSE fully-relaxed tetragonal (0, t-BiVO$_4$), the low-symmetry DFT-HSE fully-relaxed monoclinic (1, m-BiVO$_4$) to 5 additional structures with the noted magnitude of monoclinic distortion. (b) Hole effective mass at the Γ–V VBM for the 7 structures. The upper axis shows the monoclinic ratio (a/b) for comparison with experimental values in Fig. 5, and the monoclinic ratio of the Bi–V–Mo–Gd alloy with highest P_{max} is shown with a dotted line.

Conclusions

Through combinatorial alloying of P, Ca, Mo, Eu, Gd, W and their pairwise combinations into m-BiVO$_4$, several co-alloying systems were identified to be synergistic, and the photoanode performance of the best co-alloys exceeded that obtained with either alloying element individually. The best PEC performance was observed in the (Mo,Gd) system, where isovalent Gd substitution onto the Bi site and electron-donating substitution of

Mo onto the V site yields a greatly improved *J–E* curve. By using XRD to ensure m-BiVO$_4$ phase purity and Raman spectroscopy to characterize the monoclinic distortion, we identified a relationship between lowered monoclinic distortion and improved photoactivity, culminating with a Vegard-style analysis revealing that the synergy between the co-alloying elements is well explained by the anomalous lowering of the monoclinic distortion when they are combined in m-BiVO$_4$. First principles DFT calculations revealed that hole effective mass decreases with lowered monoclinic distortion and can rationalize the experimental trends. This effect is complementary to the well-established electronic conductivity increase provided by Mo and/or W alloying, providing a new mechanism by which BiVO$_4$-based photoanodes can be understood and optimized. The collective results motivate critical evaluation of the community's assumed superiority of m-BiVO$_4$ over t-BiVO$_4$ and provide a key example of the need for compositional tuning in high-dimension composition space to optimize multifunctional materials.

Conflicts of interest

There are no conflicts to declare.

Acknowledgements

Notes and references

1 D. D. Dionysiou, G. Li Puma, J. Ye, J. Schneider and D. Bahnemann, *Photocatalysis*, The Royal Society of Chemistry, 2016.

2 F. A. Fatwa and P. B. Sean, *J. Phys. D: Appl. Phys.*, 2017, **50**, 193002.

3 K. Tolod, S. Hernández and N. Russo, *Catalysts*, 2017, **7**, 13.

4 Y. Park, K. J. McDonald and K.-S. Choi, *Chem. Soc. Rev.*, 2013, **42**, 2321–2337.

5 I. D. Sharp, J. K. Cooper, F. M. Toma and R. Buonsanti, *ACS Energy Lett.*, 2017, **2**, 139–150.

6 Z.-F. Huang, L. Pan, J.-J. Zou, X. Zhang and L. Wang, *Nanoscale*, 2014, **6**, 14044–14063.

7 H. L. Tan, R. Amal and Y. H. Ng, *J. Mater. Chem. A*, 2017, **5**, 16498–16521.

8 C. Martinez Suarez, S. Hernández and N. Russo, *Appl. Catal., A*, 2015, **504**, 158–170.

9 S. J. a. Moniz, S. a. Shevlin, D. J. Martin, Z.-X. Guo and J. Tang, *Energy Environ. Sci.*, 2015, **8**, 731–759.

10 B. Pattengale, J. Ludwig and J. Huang, *J. Phys. Chem. C*, 2016, **120**, 1421–1427.

11 S. Tokunaga, H. Kato and A. Kudo, *Chem. Mater.*, 2001, **13**, 4624–4628.

12 A. Kudo, K. Omori and H. Kato, *J. Am. Chem. Soc.*, 1999, **121**, 11459–11467.

13 K. P. S. Parmar, H. J. Kang, A. Bist, P. Dua, J. S. Jang and J. S. Lee, *ChemSusChem*, 2012, **5**, 1926–1934.

14 C. P. Jiang, R. L. Wang and B. A. Parkinson, *ACS Comb. Sci.*, 2013, **15**, 639–645.

15 R. Gutkowski, C. Khare, F. Conzuelo, Y. U. Kayran, A. Ludwig and W. Schuhmann, *Energy Environ. Sci.*, 2017, **10**, 1213–1221.

16 S. Obregon and G. Colon, *Catal. Sci. Technol.*, 2014, **4**, 2042–2050.

17 H. S. Park, K. E. Kweon, H. Ye, E. Paek, G. S. Hwang and A. J. Bard, *J. Phys. Chem. C*, 2011, **115**, 17870–17879.

18 J. A. Seabold, K. Zhu and N. R. Neale, *Phys. Chem. Chem. Phys.*, 2014, **16**, 1121–1131.

19 V. Nair, C. L. Perkins, Q. Lin and M. Law, *Energy Environ. Sci.*, 2016, **9**, 1412–1429.

20 V. Jovic, J. Laverock, A. J. E. Rettie, J. S. Zhou, C. B. Mullins, V. R. Singh, B. Lamoureux, D. Wilson, T. Y. Su, B. Jovic, H. Bluhm, T. Sohnel and K. E. Smith, *J. Mater. Chem. A*, 2015, **3**, 23743–23753.

21 W. J. Jo, H. J. Kang, K.-J. Kong, Y. S. Lee, H. Park, Y. Lee, T. Buonassisi, K. K. Gleason and J. S. Lee, *Proc. Natl. Acad. Sci. U. S. A.*, 2015, **112**, 13774–13778.

22 H. S. Park, K. E. Kweon, H. Ye, E. Paek, G. S. Hwang and A. J. Bard, *J. Phys. Chem. C*, 2011, **115**, 17870–17879.

23 W. I. F. David, A. M. Glazer and A. W. Hewat, *Phase Transitions*, 1979, **1**, 155–169.

24 S. P. Berglund, A. J. E. Rettie, S. Hoang and C. B. Mullins, *Phys. Chem. Chem. Phys.*, 2012, 7065–7075.

25 L. Chen, F. M. Toma, J. K. Cooper, A. Lyon, Y. Lin, I. D. Sharp and J. W. Ager, *ChemSusChem*, 2015, **8**, 1066–1071.

26 D. Zhou, L.-X. Pang, H. Wang, J. Guo, X. Yao and C. A. Randall, *J. Mater. Chem.*, 2011, **21**, 18412–18420.

27 J. M. Gregoire, C. Xiang, X. Liu, M. Marcin and J. Jin, *Rev. Sci. Instrum.*, 2013, **84**, 024102.

28 D. Guevarra, A. Shinde, S. K. Suram, I. D. Sharp, F. M. Toma, J. A. Haber and J. M. Gregoire, *Energy Environ. Sci.*, 2016, **9**, 565–580.

29 S. Mitrovic, E. W. Cornell, M. R. Marcin, R. J. Jones, P. F. Newhouse, S. K. Suram, J. Jin and J. M. Gregoire, *Rev. Sci. Instrum.*, 2015, **86**, 013904.

30 S. K. Suram, P. F. Newhouse and J. M. Gregoire, *ACS Comb. Sci.*, 2016, **18**, 673–681.

31 G. Kresse and J. Furthmuller, *Phys. Rev. B: Condens. Matter Mater. Phys.*, 1996, **54**, 11169.

32 G. Kresse and J. Furthmuller, *Comput. Mater. Sci.*, 1996, **6**, 15–50.

33 E. N. Brothers, A. F. Izmaylov, J. O. Normand, V. Barone and G. E. Scuseria, *J. Chem. Phys.*, 2008, **129**, 011102.

34 J. P. Perdew, K. Burke and M. Ernzerhof, *Phys. Rev. Lett.*, 1996, **77**, 3865.

35 K. E. Kweon and G. S. Hwang, *Phys. Rev. B: Condens. Matter Mater. Phys.*, 2012, **86**, 165209.

36 H. J. Monkhorst and J. D. Pack, *Phys. Rev. B: Solid State*, 1976, **13**, 5188–5192.

37 G. Kresse and D. Joubert, *Phys. Rev. B: Condens. Matter Mater. Phys.*, 1999, **59**, 1758.

38 K. E. Kweon, G. S. Hwang, J. Kim, S. Kim and S. Kim, *Phys. Chem. Chem. Phys.*, 2015, **17**, 256–260.

39 K. E. Kweon and G. S. Hwang, *Phys. Rev. B: Condens. Matter Mater. Phys.*, 2013, **87**, 205202.

40 F. F. Abdi, T. J. Savenije, M. M. May, B. Dam and R. van de Krol, *J. Phys., Lett.*, 2013, **4**, 2752–2757.

41 T. W. Kim and K.-S. Choi, *Science*, 2014, **343**, 990–994.

42 A. Shinde, G. Li, L. Zhou, D. Guevarra, S. K. Suram, F. M. Toma, Q. Yan, J. A. Haber, J. B. Neaton and J. M. Gregoire, *J. Mater. Chem. A*, 2016, **4**, 14356–14363.

43 C. Zachaus, F. F. Abdi, L. M. Peter and R. van de Krol, *Chem. Sci.*, 2017, **8**, 3712–3719.

44 S. D. Kirby and R. B. van Dover, *Thin Solid Films*, 2009, **517**, 1958–1960.

45 J. K. Cooper, S. Gul, F. M. Toma, L. Chen, Y.-S. Liu, J. Guo, J. W. Ager, J. Yano and I. D. Sharp, *J. Phys. Chem. C*, 2015, **119**, 2969–2974.

46 W. Yao, H. Iwai and J. Ye, *Dalton Trans.*, 2008, 1426–1430.

47 A. Loiudice, J. Ma, W. S. Drisdell, T. M. Mattox, J. K. Cooper, T. Thao, C. Giannini, J. Yano, L.-W. Wang, I. D. Sharp and R. Buonsanti, *Adv. Mater.*, 2015, **27**, 6733–6740.

48 D. Zhou, W. G. Qu, C. A. Randall, L. X. Pang, H. Wang, X. G. Wu, J. Guo, G. Q. Zhang, L. Shui, Q. P. Wang, H. C. Liu and X. Yao, *Acta Mater.*, 2011, **59**, 1502–1509.

49 M. Gotić, S. Musić, M. Ivanda, M. Šoufek and S. Popović, *J. Mol. Struct.*, 2005, **744**, 535–540.

50 F. D. Hardcastle, I. E. Wachs, H. Eckert and D. A. Jefferson, *J. Solid State Chem.*, 1991, **90**, 194–210.

51 R. L. Frost, D. A. Henry, M. L. Weier and W. Martens, *J. Raman Spectrosc.*, 2006, **37**, 722–732.

52 V. I. Merupo, S. Velumani, G. Oza, M. Makowska-Janusik and A. Kassiba, *Mater. Sci. Semicond. Process.*, 2015, **31**, 618–623.

53 A. J. E. Rettie, W. D. Chemelewski, J. Lindemuth, J. S. McCloy, L. G. Marshall, J. S. Zhou, D. Emin and C. B. Mullins, *Appl. Phys. Lett.*, 2015, **106**, 022106.

54 A. J. E. Rettie, H. C. Lee, L. G. Marshall, J.-F. Lin, C. Capan, J. Lindemuth, J. S. McCloy, J. Zhou, A. J. Bard and C. B. Mullins, *J. Am. Chem. Soc.*, 2013, **135**, 11389–11396.

55 A. W. Sleight, H. Y. Chen, A. Ferretti and D. E. Cox, *Mater. Res. Bull.*, 1979, **14**, 1571–1581.

56 A. Walsh, Y. Yan, M. N. Huda, M. M. Al-Jassim and S. H. Wei, *Chem. Mater.*, 2009, **21**, 547–551.

57 Z. Zhao, Z. Li and Z. Zou, *Phys. Chem. Chem. Phys.*, 2011, **13**, 4746–4753.

58 K. Ding, B. Chen, Z. Fang and Y. Zhang, *Theor. Chem. Acc.*, 2013, **132**, 1352.

59 G. Li, Y. Bai and W. F. Zhang, *Mater. Chem. Phys.*, 2012, **136**, 930–934.